



Research article

Constraints-related microscopic fatigue crack propagation behaviour of polycrystalline alloys

Jie Yang^{*}, Hao-han Guo

Shanghai Key Laboratory of Multiphase Flow and Heat Transfer in Power Engineering, School of Energy and Power Engineering, University of Shanghai for Science and Technology, Shanghai, 200093, PR China

ARTICLE INFO

Keywords:

Constraint
Fatigue crack propagation
Polycrystalline alloy
Crystal plasticity
Microscopic

ABSTRACT

Based on the microscopic polycrystalline fatigue crack propagation (MPFCP) model, the MPFCP behaviours of GH4169 alloy under different micro-notch depths and lengths (constraints) were studied from aspects of MPFCP path, MPFCP rate and stress distribution. The influences of the initial crack angle on MPFCP behaviour were further explored. It was observed that the grain boundary, the grain size and the stress state were different during crack propagation under different constraints, resulting in different MPFCP paths. The MPFCP path was straighter under high constraints, and the MPFCP rate was related to the micro-notch size and the loading direction. The crack tip needed more stress accumulation at low constraints than under high constraints to ensure smooth MPFCP behaviour. The influence of the initial crack angle on the MPFCP path was mainly reflected in the grain interior where the initial crack was located. The initial crack angle had a greater influence on the MPFCP rate than on the MPFCP path.

1. Introduction

Under the continuous action of fatigue loading, stress concentration and damage accumulation initiate micro-fatigue cracks, which continue to propagate and become macro-fatigue cracks. The fatigue crack propagation (FCP) phenomenon greatly affects the service life of equipment. Therefore, it is necessary to deeply understand their FCP behaviour.

In 1957, Irwin [1] proposed the stress intensity factor “ K .” In the same year, Paris proposed that the variation range of K was the basic parameter to control the FCP rate under cyclic loading and found that the crack propagation rate (CPR) was related to the range of the stress intensity factor (ΔK). In 1963, Paris [2] proposed an exponential power law for FCP rate calculation (Paris formula). In 1967, Forman et al. [3] revised the Paris formula and summarized the Forman formula by considering the influences of average stress on da/dN and ΔK . In 1970, Elber [4] first proposed the concept of fatigue crack closure, and taken the effective stress intensity factor amplitude (K_{eff}) as the driving force of crack propagation based on the principle of plastic-induced crack closure. In 1972, Donahue et al. [5] applied the threshold stress intensity factor (K_{th}) and the constant of proportionality (A) to the description of FCP behaviour and accurately predicted the FCP rate under a corrosive environment. In 1999, McEvily et al. [6] established McEvily model to explain a variety of fatigue anomalies. In 2001, McEvily et al. [7,8] developed a single-parameter model based on a modified linear elastic fracture mechanics method. In 2003, Cui et al. [9] modified the McEvily model through a large number of experiments.

Most of the aforesaid models were based on experimental results. Gradually, the finite element method (FEM) has gradually

^{*} Corresponding author.

E-mail address: yangjie@usst.edu.cn (J. Yang).

become an important tool to study FCP behaviour. During the numerical calculation of crack propagation using FEM, the crack tip mesh is generally treated using the cohesion model, the embedded discontinuous model, the node-release technique, and the remeshing technique. At the same time, the element-free method, the boundary element method and the extended finite element method (XFEM) have also become popular. Among these methods, XFEM can solve discontinuity problems without additional mesh refinement, and was widely used to study the FCP behavior. The concept of XFEM can be traced back to Benzley's work in 1974 [10], and it was first proposed by Belytchko et al. [11]. Moës et al. [12] introduced the Heaviside step function to the unique element containing the crack surface to reflect the discontinuous characteristics of the crack and made the crack independent of the mesh. Sukumar et al. [13] supplemented the generalization of XFEM and applied it to the study of quasi-static crack propagation. Zi et al. [14] replaced the crack tip field characterization function in the form of the migration enhancement function to prove the reliability of XFEM. Kumar et al. [15] analyzed the propagation behaviours of static and dynamic cracks based on XFEM and further proposed three different enrichment function application schemes.

However, the abovementioned studies were conducted at the macro-scale. As the rise of the crystal plastic finite element method (CPFEM) [16–18], study on FCP behaviour at the micro-scale has accelerated. Pardoën et al. [19] adopted CPFEM to describe the competitive behaviour of intergranular and transgranular fractures in aluminum alloys, and established a bilayer damage model for crack propagation. Lin et al. [20] found that the crack propagation path (CPP) inside a grain tended to follow the slip surface of the grain and further predicted the FCP behaviour of polycrystalline alloys. Wilson et al. [21,22] established an FCP model with dislocation configuration stored energy as the driving force of cracks and successfully simulated the switching of slip systems and the propagation rate fluctuation of cracks in single crystals. To accurately reflect the crack deflection phenomenon under the influence of grain orientation and also to explore the influences of slip and dislocations on the crack propagation behaviour of polycrystalline alloys, based on the cumulative shear strain, the microscopic polycrystalline fatigue crack propagation (MPFCP) model has been established by combining CPFEM and XFEM [23].

Constraints are important factors affecting the fatigue behaviour of materials at both macro- and micro-scales. Constraints can be regarded as structural obstructions to the plastic deformation of materials at the crack tip. The main factors affecting constraints include specimen geometry, crack size, and material mismatch. Generally, geometric constraints are induced by specimen geometry and crack size, and the material constraint is related to material mismatch. The change of constraints greatly affects the FCP behaviour of materials. In existing standards, the FCP rate is measured using standard specimens in laboratories. But, the actual working conditions of engineering structures are often inconsistent with laboratory conditions. Moreover, different constraints lead to different crack propagation rates (CPRs). Some researchers [24–26] have proposed that a structure with high constraint has low FCP rate, whereas the opposite phenomenon also has been recorded [27]. Some studies [25,28] have observed that constraints can affect the FCP rate in both near-threshold and the Paris regions; however, some studies [26] have revealed the effect exists only in near-threshold region. Therefore, in order to accurately understand the FCP behaviour, both fatigue and constraint effects should be taken into consideration. In recent studies, the correlation between FCP rate and constraints at the macro-scale [29], the correlation between creep FCP rate and constraints at the macro-scale [30], and the correlation between fatigue crack initiation life and constraints at the micro-scale have been established, which deeply clarified the law and essence of FCP rate changing with constraints [31]. However, research on the effects of constraints on the MPFCP behaviour of polycrystalline alloys at the micro-scale is still lacking.

Based on the MPFCP model, the present work studied the constraints-related MPFCP behaviours of GH4169 alloy under different micro-notch depths and lengths (constraints), and discussed the influence of the initial crack angle on MPFCP behaviour.

2. MPFCP model and its damage criterion

2.1. Crystallographic theory

The total deformation gradient tensor \mathbf{F} is given by Equation (1).

$$\mathbf{F} = \mathbf{F}_e \cdot \mathbf{F}_p \tag{1}$$

where \mathbf{F}_e characterizes the elastic part, and \mathbf{F}_p characterizes the plastic part. The plastic rate gradient \mathbf{L}_p is given by Equation (2).

$$\mathbf{L}_p = \dot{\mathbf{F}}_p (\mathbf{F}_p)^{-1} = \sum_{\alpha} \dot{\gamma}^{\alpha} \mathbf{m}^{\alpha} \otimes \mathbf{n}^{\alpha} \tag{2}$$

where $\dot{\gamma}^{\alpha}$ represents the plastic shear strain rate, \mathbf{m}^{α} and \mathbf{n}^{α} represent the slip and normal direction respectively, and N is the number of total slip systems.

The plastic shear strain rate $\dot{\gamma}^{\alpha}$ is associated with the critical shear stress τ_c^{α} and the shear stress τ^{α} , as shown in Equation (3).

$$\dot{\gamma}^{\alpha} = f(\tau^{\alpha}, \tau_c^{\alpha} \dots) \tag{3}$$

The τ^{α} is associated with the stress state, as shown in Equation (4).

$$\tau^{\alpha} = \mathbf{S} : (\mathbf{m}^{\alpha} \otimes \mathbf{n}^{\alpha}) \tag{4}$$

\mathbf{S} is the second type of Piola-Kirchhoff stress.

The relationship between the τ_c^{α} and the $\dot{\gamma}^{\alpha}$ can be described as Equation (5).

$$\dot{\gamma}^\alpha = \dot{\gamma}_0 \text{sgn}(\tau^\alpha) \left(\frac{\tau^\alpha}{g^\alpha} \right)^n \tag{5}$$

where n is the sensitivity coefficient rate, and $\dot{\gamma}_0$ is the reference strain rate.

The total cumulative shear strain γ can be expressed as Equation (6).

$$\gamma = \sum_\alpha \int_0^t |\dot{\gamma}^\alpha| dt \tag{6}$$

Isotropic hardening mode was used, and it was achieved through the evolution of critical shear stress, as shown in Equation (7).

$$g^\alpha = \sum_\beta h^{\alpha\beta} \dot{\gamma}^\beta \tag{7}$$

g^α is the strength parameter, $\dot{\gamma}^\beta$ is the plastic slip rate, and $h^{\alpha\beta}$ is the plastic hardening matrix, which is associated with the self-hardening matrix $h^{\alpha\alpha}$, as shown in Equation (8) and Equation (9).

$$h^{\alpha\beta} = q h^{\alpha\alpha} \tag{8}$$

$$h^{\alpha\alpha} = h_0 \text{sech}^2 \left| \frac{h_0 \gamma^\alpha}{g_\infty - \tau_0} \right| \tag{9}$$

q is the latent hardening coefficient, τ_0 is the critical shear stress, h_0 is the initial hardening modulus, g_∞ represents the saturated stress.

2.2. Basics of XFEM

In XFEM, the displacement of any point is given by Equation (10).

$$\vec{\mathbf{u}} = \sum_{i=1}^N N_i(x) \left[\vec{\mathbf{u}}_i + H(x) \vec{\mathbf{a}}_i + \sum_{\alpha=1}^4 F_\alpha(x) \vec{\mathbf{b}}_i^\alpha \right] \tag{10}$$

Where $\vec{\mathbf{u}}$ is the displacement vector, $\vec{\mathbf{u}}_i$ denotes the displacement vector, $\vec{\mathbf{a}}_i$ and $\vec{\mathbf{b}}_i^\alpha$ are the vector generated, $N_i(x)$ is the shape function. $H(x)$ is the tip function which can reflect displacement discontinuity, and its value is related to a level set function $\phi(x)$, as

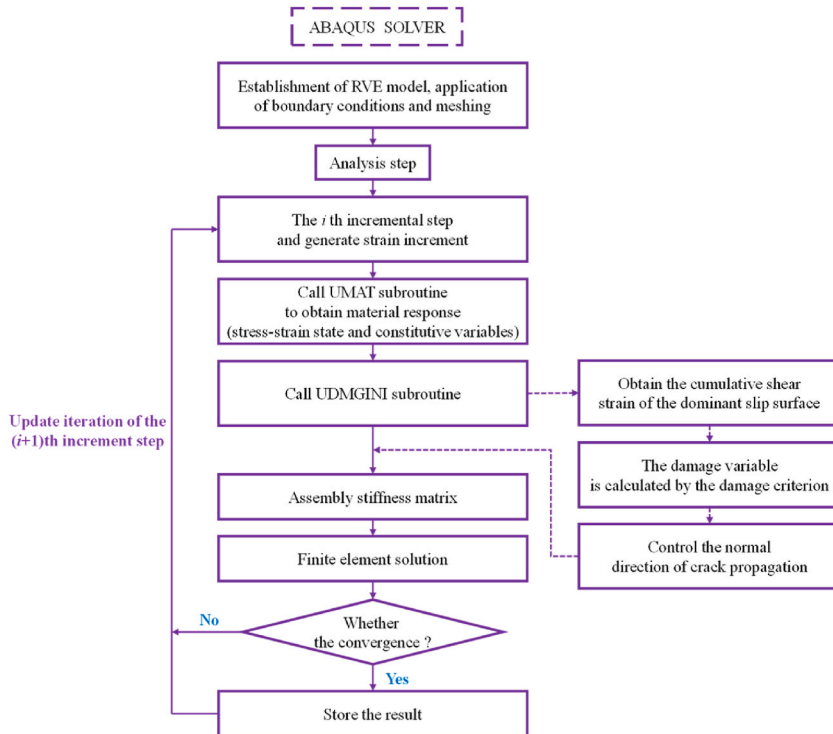


Fig. 1. Flowchart of the model [23].

shown in Equation (11).

$$H(x) = \begin{cases} 1 & \vartheta(x) > 0 \\ -1 & \vartheta(x) < 0 \end{cases} \quad (11)$$

The $F_a(x)$ can be given by Equation (12).

$$F_a(x) = \left[\sqrt{r} \sin \frac{\theta}{2}, \sqrt{r} \cos \frac{\theta}{2}, \sqrt{r} \sin \theta \sin \frac{\theta}{2}, \sqrt{r} \sin \theta \cos \frac{\theta}{2} \right] \quad (12)$$

2.3. MPFCP model

In ABAQUS software, the theoretical framework detailed in Section 2.1 was implemented using a user-defined material subroutine (UMAT). The user-defined damage criterion subroutine (UDMGINI) was utilized in conjunction with the XFEM module detailed in Section 2.2. The damage criterion served as the basis for damage assessment. Under fatigue loading conditions for the MPFCP model, all slip surfaces became activated, the cumulative shear strains on the 12 slip systems were computed and compared. The slip system experiencing the largest cumulative shear strain was designated as the dominant slip system (α). When the γ_α to the γ_{cr} on the most active slip system reached unity, the element located ahead of the crack tip fractured, as expressed in Equation (13) [23].

$$\frac{\gamma_\alpha}{\gamma_{cr}} = 1 \quad (13)$$

The model described above was implemented within ABAQUS software, and the flowchart of this model is listed in Fig. 1 [23].

3. Finite element modeling and scheme design

3.1. Material

GH4169 alloy (precipitated phase strengthening material used in aerospace equipment) was selected as the research object. Each independent grain in the representative volume element (RVE) of this alloy was a face-centered cubic (FCC) structure. The constitutive parameters and chemical composition are showed in Table 1 and Table 2 [32].

3.2. Establishment of RVE

The two-dimensional RVE was created using the Voronoi Tessellation method [33] (Fig. 2). This RVE had an overall size of 200 μm \times 200 μm , which contained 150 grains and 23,729 elements, and can exhibited good stability results [20]. All grains were randomly oriented according to electron backscatter diffraction results.

3.3. Scheme design

To study the effect of different constraint conditions on the MPFCP behaviour of GH4169 alloy, micro-notches of different sizes were set in the middle of the right boundary of the model shown in Fig. 2 (Fig. 3, where a and b are the depth and length of the micro-notch, respectively). Different constraints were obtained by changing the micro-notch depth ($a = 15, 30, 45, 60, 75, 90, 105, 120,$ and $135 \mu\text{m}$) and length ($b = 15, 30, 45, 60,$ and $75 \mu\text{m}$). The micro-notch length was kept fixed to 15 μm when the micro-notch depth was changed, and the micro-notch depth was kept fixed to 15 μm when the micro-notch length was changed.

Generally, the upper-left and lower-left corners of rectangular micro-notches are potential locations for fatigue crack initiation [34–36], and it was well reflected in the normalization verification of the local peak stress distribution in the first fatigue cycle of the micro-notched specimens of different lengths (Fig. 4). The stress extraction at the micro-notch is displayed in Fig. 4(a), where the initial point is located in the upper-left corner of the notch, the end point is located in the lower-left corner of the notch, and the reference point is located at the center of the stress extraction path. It is noticeable from Fig. 4(b) that the maximum stress values at the initial and end points of the normalized stress-normalized distance curves of the micro-notched specimens of different lengths were 1.6–2.2 times higher than those in the central position. Moreover, the stress values at the end point of the specimens were slightly larger than those at the initial point. Therefore, the initial crack was prefabricated at the end point for all specimens. The left boundary of the micro-notch was taken as the reference edge, and an initial crack with a length of 1 μm and a counter-clockwise direction of 135° was prefabricated (Fig. 3). To further analyze the influences of the initial crack angle on MPFCP behaviour, initial cracks with three different angles (45°, 90°, and 135°) were set (Fig. 5).

Table 1
Constitutive parameters of GH4169 alloy [32].

| C_{11} /GPa | C_{12} /GPa | C_{44} /GPa | $\dot{\gamma}_0$ | n | g_{∞} /MPa | h_0 /MPa | τ_0 /MPa |
|---------------|---------------|---------------|------------------|-----|-------------------|------------|---------------|
| 266 | 114 | 76 | 1E-5 | 10 | 650 | 200 | 315 |

Table 2
Chemical composition of GH4169 alloy (wt%) [32].

| C | Ti | Al | Fe | Si | Mb | Nb | Cr | Ni |
|------|------|------|-------|------|------|------|-------|---------|
| 0.82 | 1.16 | 0.44 | 18.93 | 0.18 | 2.74 | 5.19 | 19.55 | Balance |

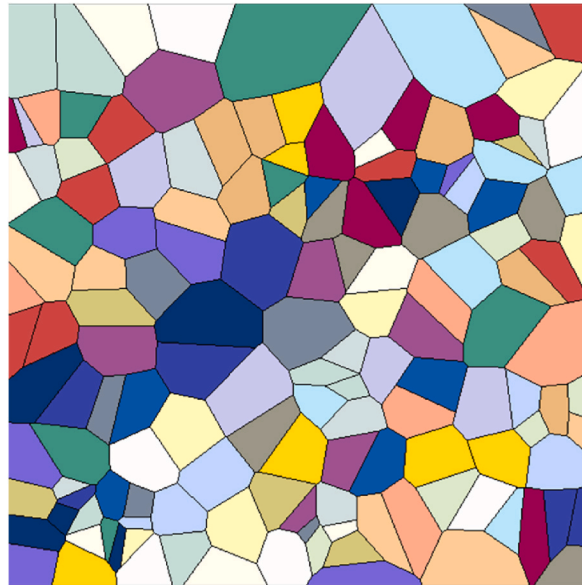


Fig. 2. RVE for GH4169 alloy.

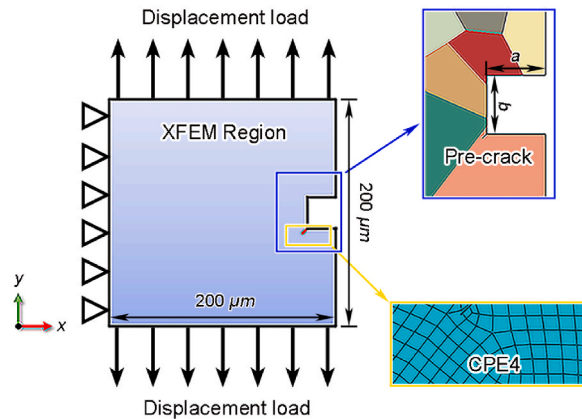


Fig. 3. Schematic of model loading and geometry (a —micro-notch depth, b —micro-notch length).

3.4. Finite element modeling

Python language was used to analyze the topological information and grain orientation of the Voronoi diagram, and the two-dimensional polycrystalline geometric model was generated in ABAQUS software. Apply displacement loads at the top and bottom of the model. The total strain amplitude and the loading ratio (R_e) were precisely set to 0.12 % and 0, respectively. The fatigue loading waveform was designed to be triangular in shape. Additionally, to eliminate any potential influence of rigid body displacement, the displacement of the left boundary along the x -direction was strictly constrained.

Four-node plane strain elements (CPE4) were selected for the meshing of the entire model. To solve grid dependence on calculation results, different mesh sizes were selected (1.5, 1, and 0.8 μm) (Fig. 6). When the mesh size was reduced to 1 μm , it was observed that the calculation results became insensitive to further changes in mesh size. Therefore, the mesh size was ultimately set to 1 μm . Because the total cumulative shear strain increases linearly, a small critical value was employed for each group of specimens to assess the

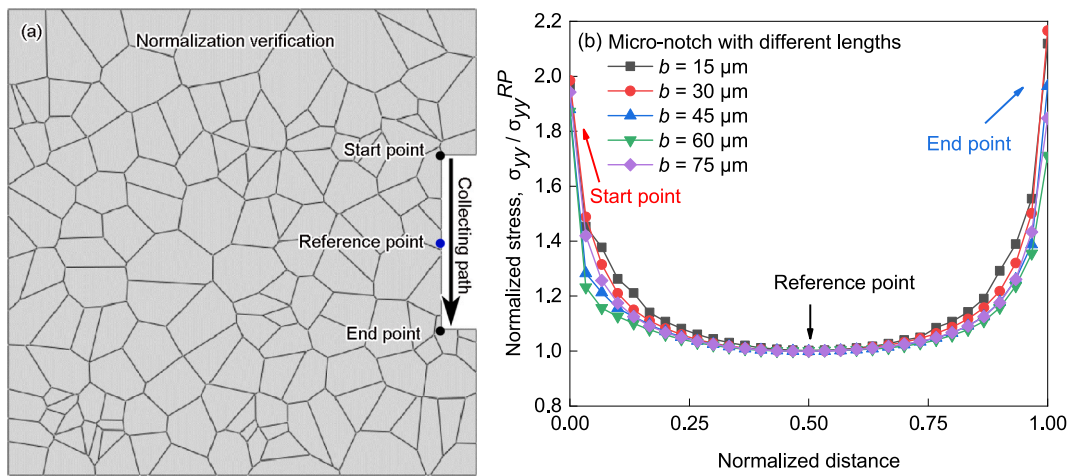


Fig. 4. (a) Schematic of stress extraction along the collecting path, and (b) relationship between normalized stress and normalized distance along the collecting path.

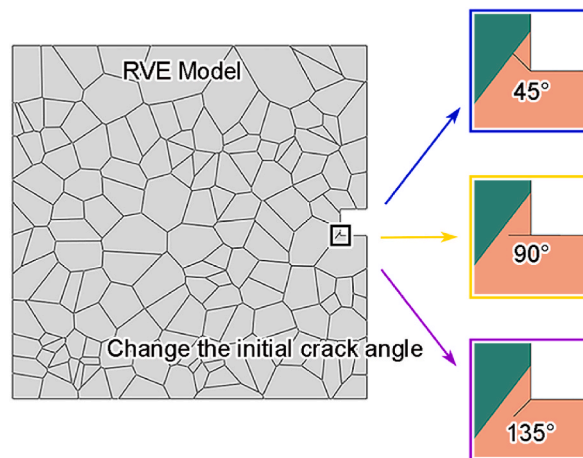


Fig. 5. RVE models containing initial cracks.

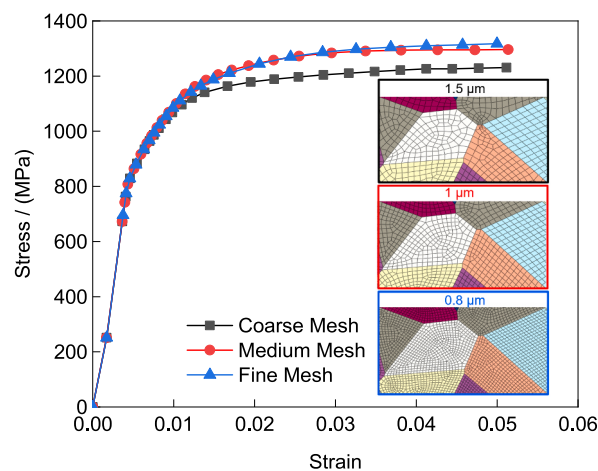


Fig. 6. Stress-strain curves for different mesh sizes.

propagation behaviour of the element in front of the crack tip, and the critical total shear strain (γ_{cr}) was set to $1E-10$ [23].

4. Results and discussion

4.1. Influences of constraints on MPFCP behaviour

4.1.1. Micro-notch depths

When the initial crack angle was 135° , the crack propagation paths (CPPs) of the nine specimens with various micro-notch depths ($a = 15, 30, 45, 60, 75, 90, 105, 120,$ and $135 \mu\text{m}$) are presented in Fig. 7. It is noticeable that the CPPs were different at different micro-notch depths, and the reason for this occurrence is that during crack propagation, grain boundaries and grains respond differently to various constraints. When the crack encounters a grain boundary, its propagation direction is deflected based on the distinct grain orientations. At the micro-scale, crack propagation is heavily effected by grain orientation. Furthermore, when cracks of varying lengths traverse the same grain, their CPPs vary due to distinct crack tip stresses under various constraints. The specimens with high micro-notch depths (Fig. 7(f), (g), 7(h), and 7(i)) had larger crack tip stress and straighter CPPs than the specimens with low micro-notch depths (Fig. 7(a), (b), 7(c), 7(d), and 7(e)).

Moreover, when the crack passed through an individual grain, (grain A in Fig. 7(c)), its propagation path was deflected slightly, and it happened due to the strong competition of slip systems inside the grain. In the entire crack propagation process, both transgranular and intergranular fractures coexisted; however, the transgranular fracture was more dominant in the alloy.

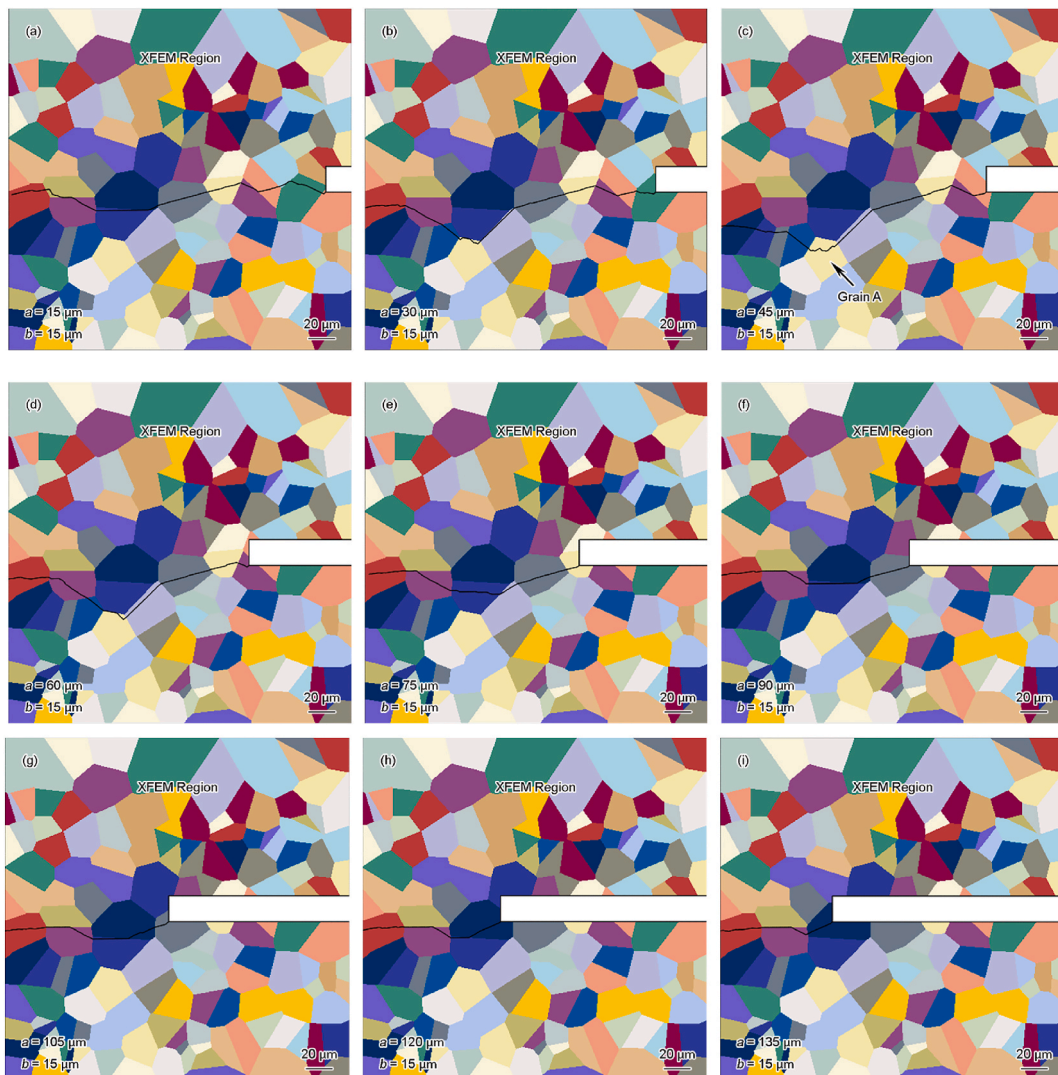


Fig. 7. MPFCP paths of the specimens with different micro-notch depths: (a) $a = 15 \mu\text{m}$, (b) $a = 30 \mu\text{m}$, (c) $a = 45 \mu\text{m}$, (d) $a = 60 \mu\text{m}$, (e) $a = 75 \mu\text{m}$, (f) $a = 90 \mu\text{m}$, (g) $a = 105 \mu\text{m}$, (h) $a = 120 \mu\text{m}$, and (i) $a = 135 \mu\text{m}$.

Fig. 8 presents the relationship between the cycle number and length of MPFCP for the specimens with different micro-notch depths and also the cycle number when the crack propagation length reached 50 μm . It is evidence from Fig. 8(a) that with increase in micro-notch depth, the cycle number gradually decreased, and the CPR increased. When the micro-notch depth reached a certain value, the CPR tended to be stable, indicating that micro-notch depth had a promoting effect on the MPFCP rate.

The regularity reflected in Fig. 8(b) is consistent with that in Fig. 8(a). When the length of MPFCP reached 50 μm , the cycle number decreased with the increase in micro-notch depth. When the length of MPFCP reached 90 μm , the cycle number reached the minimum, and the CPR reached the maximum. Subsequently, the cycle number increased slightly with the increase in the length of MPFCP. Generally, in the macro-scale, high constraint may decrease or increase the FCP rate [24,27], which was depended on the different loading modes [29]. However, this study reveals the MPFCP rate gradually increased with the increasing in constraint at the micro-scale.

When the length of MPFCP reached 60 μm , the Mises stress distributions of the specimens with different micro-notch depths ($a = 15 \mu\text{m}$, $75 \mu\text{m}$, and $135 \mu\text{m}$) are exhibited in Fig. 9. In the three specimens shown in Fig. 7(a), (e), and Fig. 7(i), high stress concentration regions were formed at grain boundaries, and it happened because high-stress regions could be easily formed near grain boundaries than inside grains. When the micro-notch depth was $15 \mu\text{m}$ (Fig. 9(a)), stress concentration was more obvious, and the stress value was relatively high. When the micro-notch depths were $75 \mu\text{m}$ (Fig. 9(b)) and $135 \mu\text{m}$ (Fig. 9(c)), stress concentrations at the crack tip were less severe and the stress values were lower, indicating that the crack tip required larger stress accumulation to ensure smooth MPFCP behaviour at the low constraint, whereas at the high constraint, relatively smaller stress accumulation could realize crack propagation, and the regularity was consistent with that shown in Fig. 8(b).

4.1.2. Micro-notch lengths

When the initial crack angle was 135° , the CPPs of the five specimens with different micro-notch lengths ($b = 15, 30, 45, 60,$ and $75 \mu\text{m}$) are displayed in Fig. 10 (specimen with $b = 15 \mu\text{m}$ is shown in Fig. 7(a)). Consistent with Fig. 7, the crack growth process was accompanied by transgranular and intergranular fractures, but dominant in the transgranular fracture. With the increase in micro-notch length (from Fig. 10(a), (b), 10(c) to 10(d)), grain boundaries and grains through which the crack propagated changed noticeably.

Fig. 11 presents the relationship between the length of MPFCP and the cycle number for the specimens with different micro-notch lengths and also the cycle number when the crack propagation length reached 50 μm . It is noticeable from Fig. 11(a) that with the increase in the micro-notch length, the CPR first increased and then decreased. When the micro-notch length was 30 μm , the CPR reached the maximum. With the further increase in micro-notch length, the CPR started to decrease, which was related to the consistency between the changing direction in micro notch length and the loading direction. With the increase in micro-notch length, the strain along the loading direction was averaged, and the strain variation range was reduced [28]. The regularity reflected in Fig. 11(b) is consistent with that in Fig. 11(a). When the length of MPFCP reached 50 μm , the cycle number was the minimum. In the case of the micro-notch length was 30 μm , as the length of micro-notches continues to increase, the cycle number increased rapidly.

When the length of MPFCP reached 100 μm , the Mises stress distributions of the specimens with different micro-notch lengths ($b = 15 \mu\text{m}$, $45 \mu\text{m}$, and $75 \mu\text{m}$) are exhibited in Fig. 12. Compared with Figs. 7(a)–10(b) and (d), it can be found that stress concentration tended to occurred at grain boundaries, and it is consistent with the phenomenon observed in Fig. 9. With the increase in micro-notch length (from Fig. 12(a) and (b) to 12(c)), stress concentration became more obvious both at the crack tip and along the CPP, indicating that the crack required larger stress to ensure smooth MPFCP behaviour; thus, the CPR decreased, and the cycle number gradually increased.

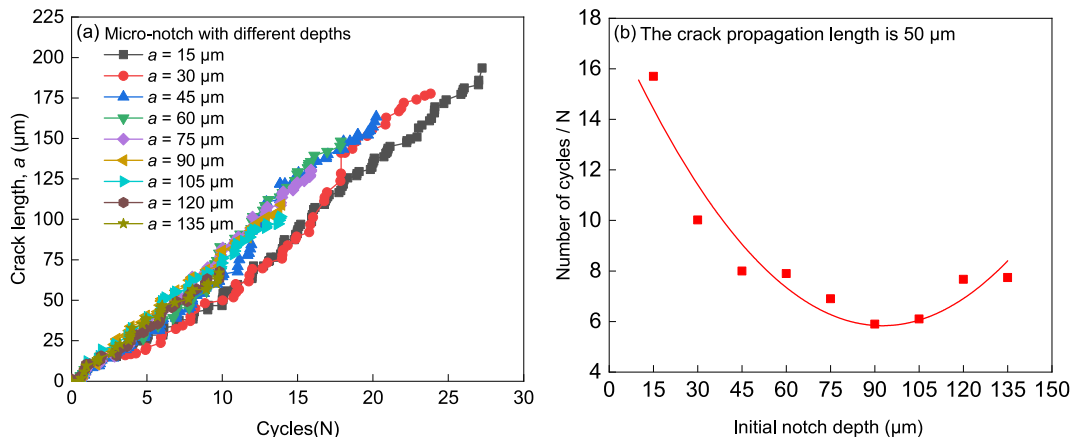


Fig. 8. (a) Relationship between the cycle number and length of MPFCP, and (b) the cycle number when the length of MPFCP reached 50 μm .

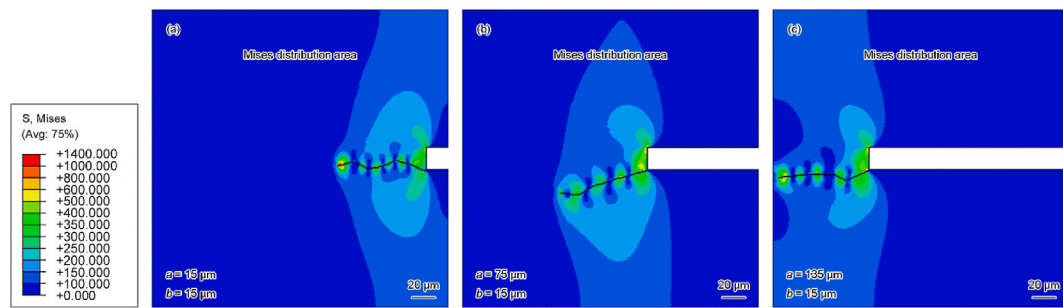


Fig. 9. Mises stress distributions of the specimens with different micro-notch depths when the length of MPFCP reached 60 μm : (a) $a = 15 \mu\text{m}$, (b) $a = 75 \mu\text{m}$, and (c) $a = 135 \mu\text{m}$.

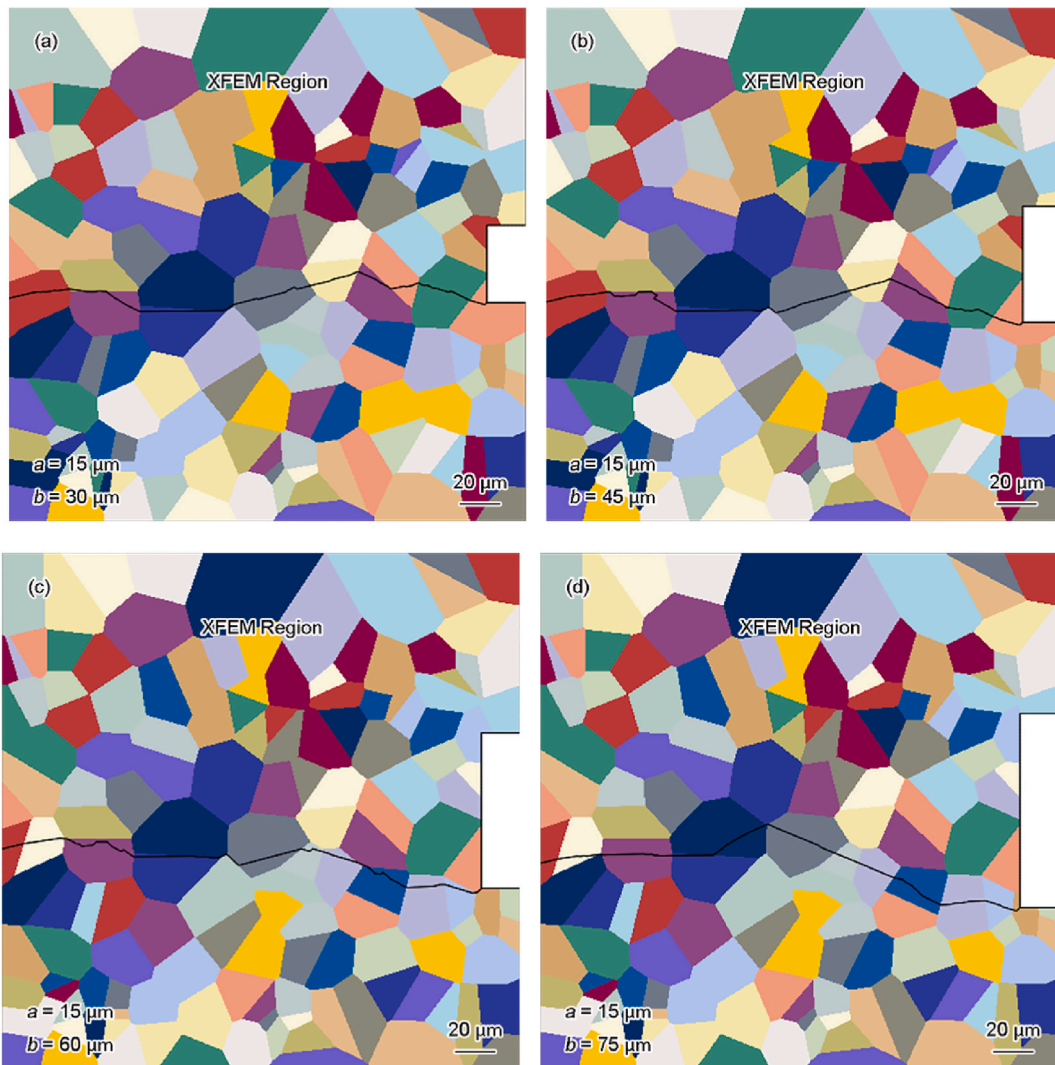


Fig. 10. MPFCP paths of the specimens with different micro-notch lengths: (a) $b = 30 \mu\text{m}$, (b) $b = 45 \mu\text{m}$, (c) $b = 60 \mu\text{m}$, and (d) $b = 75 \mu\text{m}$.

4.2. Effects of the initial crack angle on MPFCP behaviour

Fig. 13 displays the CPPs of the micro-notched specimens containing initial cracks at different angles (45° , 90° , and 135°) under three different constraints ($a = 15 \mu\text{m}$ and $b = 15 \mu\text{m}$; $a = 135 \mu\text{m}$ and $b = 15 \mu\text{m}$; and $a = 15 \mu\text{m}$ and $b = 75 \mu\text{m}$). As the length of initial

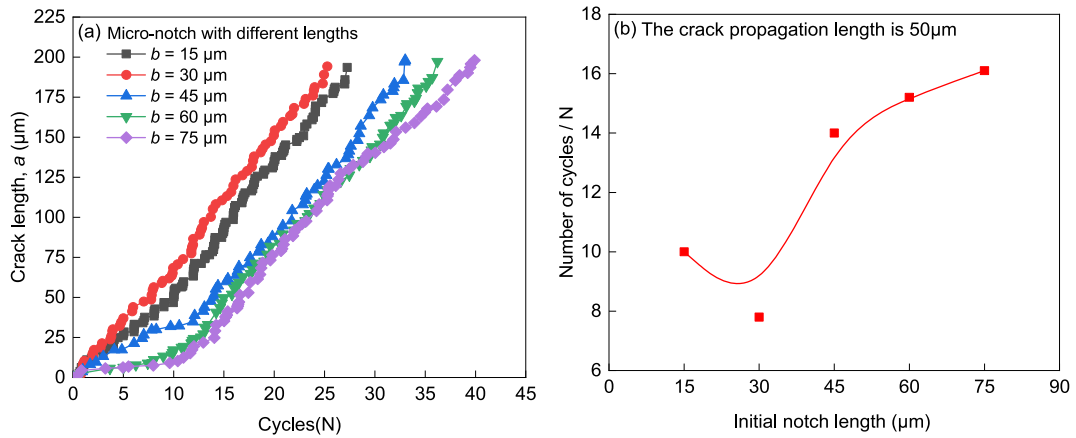


Fig. 11. (a) Relationship between the cycle number and length of MPFCP, and (b) the cycle number when the length of MPFCP reached 50 μm.

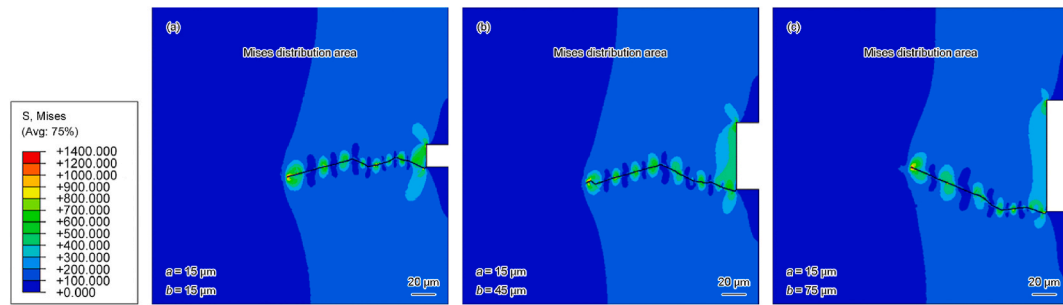


Fig. 12. Mises stress distributions of the specimens with different micro-notch lengths when the length of MPFCP reached 100 μm: (a) $b = 15 \mu\text{m}$, (b) $b = 45 \mu\text{m}$, and (c) $b = 75 \mu\text{m}$.

crack was only 1 μm, which was extremely small as compared with the overall model, no significant difference in the CPPs of the specimens was noticed. The influence of the initial crack angle on the CPP was mainly reflected in the grain interior where the initial crack was located (Fig. 15).

Fig. 14 presents the relationship between the cycle number and length of MPFCP for the micro-notched specimens containing initial cracks at different angles. It is observable from Fig. 14(a) that the micro-notched specimen with $a = 15 \mu\text{m}$ and $b = 15 \mu\text{m}$, when the initial crack angles were 45° and 135° , the CPR was faster, and fewer cycles were required as compared with the case with the initial crack angle of 90° . It happened because the micro-notch shape was square and the crack was located in the middle of the specimen. According to Schmid’s slip law, as the slip direction becomes more parallel to the tensile direction, the chance of slip will increase. Therefore, as compared with the case with the initial angle of 90° , in the specimens with the initial crack angles of 45° and 135° , slip easily occurred, and the crack freely propagated. It is noticeable from Fig. 13(a), (b), and 13(c), at the beginning of the propagation process, the crack propagated upward at 45° , and this phenomenon is consistent with the case for the initial crack angle of 45° . Therefore, the CPR at the initial crack angle of 45° was faster than that at 135° .

It is evident from Fig. 14(b) that for the micro-notched specimen with $a = 135 \mu\text{m}$ and $b = 15 \mu\text{m}$ (corresponding Fig. 13(d), (e), and 13(f) for CPP), the propagation rate was the fastest when the initial crack angle was 135° . In this case, although the shape of the micro-notch changed, the crack was still located in the middle of the specimen, the slip was more prone to occur at 45° and 135° . Moreover, it is clear from Fig. 15 that at the beginning of crack propagation, the initial crack propagated downward at 135° in the first grain; thus, the CPR was the fastest when the initial crack angle was 135° .

It is observable from Fig. 14(c) that for the micro-notched specimen with $a = 15 \mu\text{m}$ and $b = 75 \mu\text{m}$, the propagation rate was the fastest when the initial crack angle was 45° . In this case, the shape of the micro-notch changed, and the crack was located in the lower half of the specimen. As the tensile load acted on both the upper and lower sides of the specimen, the crack tended to propagate along the horizontal center line of the specimen. The crack experienced an upward propagation trend, and it is consistent with the CPPs shown in Fig. 13(g), (h), and 13(i). It is clear from Fig. 13(g), (h), and 13(i) that the crack gradually approached the center line and propagated forward along this line. Moreover, the slip in this direction also followed Schmid’s slip law.

To further analyze the influence of the initial crack angle, a micro-notched specimen with $a = 135 \mu\text{m}$ and $b = 15 \mu\text{m}$ was selected. When the grain where the initial crack was located cracked completely, the stress distributions and CPPs of the micro-notched specimens were investigated (Fig. 15). It was found that when the initial crack angle was 90° (Fig. 15(b)), the stress concentration was the highest, the stress accumulation required for crack propagation was the largest, and the CPR was the slowest. When the initial

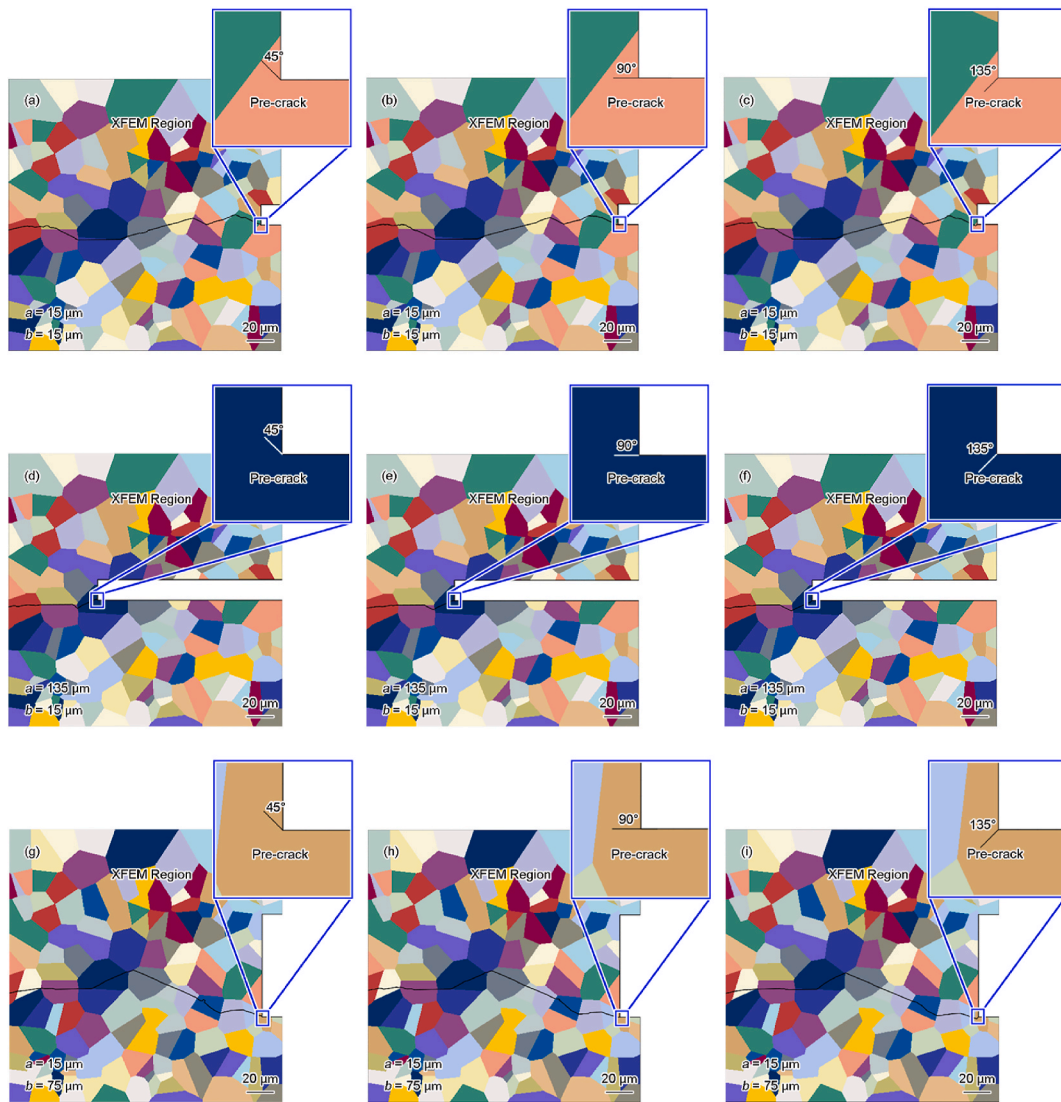


Fig. 13. MPFCP paths of the micro-notched specimens containing initial cracks at different angles: $a = 15 \mu\text{m}$ and $b = 15 \mu\text{m}$, (a) 45° , (b) 90° , (c) 135° ; $a = 135 \mu\text{m}$ and $b = 15 \mu\text{m}$, (d) 45° , (e) 90° , (f) 135° ; and $a = 15 \mu\text{m}$ and $b = 75 \mu\text{m}$, (g) 45° , (h) 90° , (i) 135° .

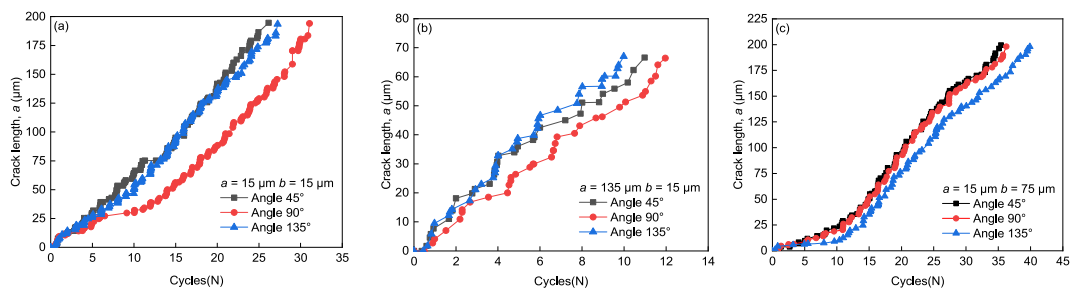


Fig. 14. Relationship between the cycle number and Length of MPFCP for the micro-notched specimens containing initial cracks at different angles: (a) $a = 15 \mu\text{m}$, $b = 15 \mu\text{m}$, (b) $a = 135 \mu\text{m}$, $b = 15 \mu\text{m}$, and (c) $a = 15 \mu\text{m}$, $b = 75 \mu\text{m}$.

crack angle was 135° (Fig. 15(c)), the stress concentration was lower and the CPR was faster than the cases with the initial crack angle of 45° (Fig. 15(a)), and this phenomenon is consistent with the case shown in Fig. 14(b). Which was also the essence of the change of CPP in Fig. 13 and CPR in Fig. 14.



Fig. 15. Stress distributions and CPPs of the micro-notched specimens containing initial cracks at three different angles: (a) 45°, (b) 90°, and (c) 135°.

5. Conclusions

The MPFCP behaviours of GH4169 alloy under different micro-notch depths and lengths (constraints) were studied, and the influences of the initial crack angle on MPFCP behaviour were further explored. The main findings are summarized below.

- (1) The MPFCP path changed with the increase in micro-notch depth and length, and it happened because the grain boundary, the grain size, and the stress state at the crack tip were different during crack propagation under different constraints. The CPP was straighter under high constraints.
- (2) With the increase in micro-notch depth, the CPR first increased and then became stable, whereas with the increase in micro-notch length, the CPR first increased and then decreased. The CPR was related to the micro-notch size and the loading direction. The crack tip required more stress accumulation at low constraints than under high constraints to ensure smooth MPFCP behaviour.
- (3) The influence of the initial crack angle on the MPFCP path was mainly reflected in the grain interior where the initial crack was located. The initial crack angle had a great effect on the MPFCP rate than on the MPFCP path. When the crack was located in the middle of the specimen, and the initial crack angles were 45° and 135°, slip easily occurred, and the crack propagated freely as compared with the case with the initial crack angle of 90°, which followed the Schmid's slip law. When the crack was located on one side of the specimen, it tended to propagate toward the horizontal center line of the specimen.
- (4) The MPFCP model developed based on CPFEM and XFEM successfully realized the MPFCP behaviour of polycrystalline alloys. The damage criterion based on the cumulative shear strain on each slip system could better reflect the slip-dominated FCP mechanism at the micro-scale.

CRedit authorship contribution statement

Jie Yang: Writing – review & editing, Writing – original draft, Visualization, Validation, Software, Methodology, Formal analysis.
Hao-han Guo: Writing – original draft, Validation, Software.

Declaration of competing interest

The authors declare that they have no known competing financial interests or personal relationships that could have appeared to influence the work reported in this paper.

Acknowledgements

This project is sponsored by National Natural Science Foundation of China (Grant Nos. 52375154, 51975378 and 52311530067) and Shanghai Pujiang Program (Grant No. 21PJD047).

References

- [1] G.R. Irwin, Analysis of stresses and strains near the end of a crack traversing a plate, *J. Appl. Mech.* 24 (1957) 361–364.
- [2] P. Pairs, F. Erdogan, A critical analysis of crack propagation laws, *Journal of Basic Engineering* 85 (1963) 528–533.
- [3] R.G. Forman, V.E. Kearney, R.M. Engle, Numerical analysis of crack propagation in cyclic-loaded structures, *Journal of Basic Engineering* 89 (1967) 459–463.
- [4] W. Elber, Fatigue crack closure under cyclic tension, *Eng. Fract. Mech.* 2 (1) (1970) 37–45.
- [5] R.J. Donahue, H.M. Clark, P. Atanmo, et al., Crack opening displacement and the rate of fatigue crack growth, *Int. J. Fract. Mech.* 8 (1972) 209–219.
- [6] A.J. McEvily, A modified constitutive relation for fatigue crack growth [C], in: *Proceedings of the 7th International Fatigue Congress*, vol. 99, Higher Education Press, 1999, pp. 329–336.
- [7] A.J. McEvily, S. Ishihara, On the dependence of the rate of fatigue crack growth on the $\sigma_{an}(2a)$ parameter, *Int. J. Fatig.* 23 (2) (2001) 115–120.
- [8] S. Ishihara, A.J. McEvily, Analysis of short fatigue crack growth in cast aluminum alloys, *Int. J. Fatig.* 24 (11) (2002) 1169–1174.
- [9] W.C. Cui, X.P. Huang, A general constitutive relation for fatigue crack growth analysis of metal structures, *Acta Metall. Sin.* 16 (5) (2003) 342–354.
- [10] S.E. Benzley, Representation of singularities with isoparametric finite elements, *Int. J. Numer. Methods Eng.* 8 (3) (1974) 537–545.
- [11] T. Belytschko, T. Black, Elastic crack growth in finite elements with minimal remeshing, *Int. J. Numer. Methods Eng.* 45 (5) (1999) 601–620.
- [12] N. Moës, J. Dolbow, T. Belytschko, A finite element method for crack growth without remeshing, *Int. J. Numer. Methods Eng.* 46 (1) (1999) 131–150.
- [13] N. Sukumar, Z.Y. Huang, J.H. Prevost, et al., Partition of unity enrichment for bimaterial interface cracks, *Int. J. Numer. Methods Eng.* 59 (8) (2004) 1075–1102.

- [14] G. Zi, T. Belytschko, New crack-tip elements for xFEM and applications to cohesive cracks, *Int. J. Numer. Methods Eng.* 57 (15) (2003) 2221–2240.
- [15] S. Kumar, I.V. Singh, B.K. Mishra, et al., New enrichment in XFEM to model dynamic crack response of 2-D elastic solids, *Int. J. Impact Eng.* 87 (2016) 198–211.
- [16] Y.G. Huang, A User-Material Subroutine Incorporating Single Crystal Plasticity in the ABAQUS Finite Element Program [M], Harvard University, 1991.
- [17] F. Roters, P. Eisenlohr, L. Hantcherli, et al., Overview of constitutive laws, kinematics, homogenization and multiscale methods in crystal plasticity finite-element modeling: Theory, experiments, applications, *Acta Mater.* 58 (4) (2010) 1152–1211.
- [18] F. Roters, P. Eisenlohr, T.R. Bieler, et al., *Crystal Plasticity Finite Element Methods: in Materials Science and Engineering* [M], Wiley-VCH Verlag, 2010.
- [19] T. Pardoen, D. Dumont, A. Deschamps, et al., Grain boundary versus transgranular ductile failure, *J. Mech. Phys. Solid.* 51 (4) (2003) 637–665.
- [20] B. Lin, L.G. Zhao, J. Tong, A crystal plasticity study of cyclic constitutive behaviour, crack-tip deformation and crack-growth path for a polycrystalline nickel-based superalloy, *Eng. Fract. Mech.* 78 (10) (2011) 2174–2192.
- [21] D. Wilson, F.P.E. Dunne, A mechanistic modelling methodology for microstructure-sensitive fatigue crack growth, *J. Mech. Phys. Solid.* 124 (2019) 827–848.
- [22] D. Wilson, W. Wan, F.P.E. Dunne, Microstructurally-sensitive fatigue crack growth in HCP, BCC and FCC polycrystals, *J. Mech. Phys. Solid.* 126 (2019) 204–225.
- [23] H.H. Guo, R.S. Lu, F. Liu, et al., Microscopic fatigue crack propagation model for polycrystalline alloys, *Int. J. Fatig.* 170 (2023) 107526.
- [24] I. Varfolomeev, M. Luke, S. Moroz, Experimental and numerical investigations of fatigue crack growth in various specimen geometries, *Procedia Eng.* 2 (1) (2010) 1829–1837.
- [25] P. Hutař, S. Seitl, Z. Knésl, Effect of constraint on fatigue crack propagation near threshold in medium carbon steel, *Comput. Mater. Sci.* 37 (1–2) (2006) 51–57.
- [26] P. Hutař, S. Seitl, T. Kruml, Effect of specimen geometry on fatigue crack propagation in threshold region, in: *In the 12th International Conference on Fracture*, vol. 4, 2009, p. 2914. Ottawa.
- [27] J. Tong, T-stress and its implications for crack growth, *Eng. Fract. Mech.* 69 (12) (2002) 1325–1337.
- [28] S. Seitl, P. Hutař, Fatigue-crack propagation near a threshold region in the framework of two-parameter fracture mechanics, *Materiali in tehnologije* 41 (3) (2007) 135–138.
- [29] J. Yang, G.L. Guo, R.S. Lu, et al., Numerical modelling of a new FCP model and a correlation of the FCP rate with the constraint, *Int. J. Fatig.* 163 (2022) 107036.
- [30] R.S. Lu, J.P. Tan, J. Yang, et al., A new creep-fatigue crack growth model and a correlation of the creep-fatigue crack growth rate with unified constraint parameter, *Int. J. Fatig.* 166 (2023) 107248.
- [31] H.H. Guo, J. Yang, F. Liu, et al., Constraint related fatigue crack initiation life of GH4169 superalloy, *Acta Metall. Sin.* 58 (12) (2022) 1633–1644.
- [32] G.J. Yuan, X.C. Zhang, B. Chen, et al., Low-cycle fatigue life prediction of a polycrystalline nickel-base superalloy using crystal plasticity modelling approach, *J. Mater. Sci. Technol.* 38 (2020) 28–38.
- [33] F. Barbe, L. Decker, D. Jeulin, et al., Intergranular and intragranular behavior of polycrystalline aggregates. Part 1: FE model, *Int. J. Plast.* 17 (4) (2001) 513–536.
- [34] I. Pöllänen, H. Martikka, Fatigue endurance dimensioning by strain life method with a novel notch coefficient, *Mach. Des.* 2010 (2010) 43–48.
- [35] H. Hallberg, S.K. Ås, B. Skallerud, Crystal plasticity modeling of microstructure influence on fatigue crack initiation in extruded Al6082-T6 with surface irregularities, *Int. J. Fatig.* 111 (2018) 16–32.
- [36] R.Z. Wang, H.H. Gu, S.P. Zhu, et al., A data-driven roadmap for creep-fatigue reliability assessment and its implementation in low-pressure turbine disk at elevated temperatures, *Reliab. Eng. Syst. Saf.* 225 (2022) 108523.